Nature Communications

https://doi.org/10.1038/s41467-026-70993-0

Article in Press

Efficient Pt_1Ni single-atom alloy catalyst for hydrogen-free catalytic fractionation of lignocellulose

Received: 4 November 2025

Accepted: 11 March 2026

Cite this article as: Zhou, H., Xiang, Q., Guo, Z. *et al.* Efficient Pt_1Ni single-atom alloy catalyst for hydrogen-free catalytic fractionation of lignocellulose. *Nat Commun* (2026). https://doi.org/10.1038/s41467-026-70993-0

Hao Zhou, Qian Xiang, Zhiruo Guo, Kepeng Song, Mohsen Shakouri, Yong Guo, Xiaohui Liu, Yongfeng Hu, Xiao-Ming Cao & Yanqin Wang

Efficient Pt_1Ni single-atom alloy catalyst for hydrogen-free catalytic fractionation of lignocellulose

Hao Zhou[a,b†], Qian Xiang[a†], Zhiruo Guo[a†], Kepeng Song[c†], Mohsen Shakouri[d], Yong Guo[a], Xiaohui Liu[a], Yongfeng Hu[e], Xiao-Ming Cao[f]*, Yanqin Wang[a]*

[a] State key laboratory of green chemical engineering and industrial catalysis, Research Institute of Industrial Catalysis, School of Chemistry and Molecular Engineering, East China University of Science and Technology, 130 Meilong Road, Shanghai, P. R. China.

[b] School of Environmental and Nature Resources, Zhejiang University of Science and Technology, Hangzhou, Zhejiang 310023, China.

[c] Electron microscopy centre, Shandong University, 27 ShandaNan Road, Jinan, P. R. China.

[d] Canadian Light Source Inc., Saskatoon, Saskatchewan S7N 2V3, Canada.

[e] Sinopec Shanghai Research Institute of Petrochemical Technology, Shanghai 201208, China.

[f] State Key Laboratory of Synergistic Chem-Bio Synthesis, School of Chemistry and Chemical Engineering, Shanghai Jiao Tong University, Shanghai 200240, P. R. China.

[†] These four authors contribute equally to this work.

*Corresponding authors: xmcao@sjtu.edu.cn; wangyanqin@ecust.edu.cn

Abstract:

The production of monophenols from lignocellulose with cellulose intact without exogenous hydrogen *via* self-hydrogen supplied fractionation is promising, yet requires high metal loadings and yields saturated products. Herein, we report a single-atom alloyed Pt_1Ni catalyst that achieves 50.9 wt% yield of phenolic monomers from birch sawdust with about 50% selectivity to valuable propenyl side-chained products under mild conditions (140 °C, 1 atm N_2), while preserving cellulose intact. Reaction pathway studies and density functional theory calculations based on a β-O-4 model compound reveal three coexisting pathways. The Pt_1Ni alloy preferentially promotes the dehydroxylation of C_α-OH and forms a key C_α=C_β intermediate due to the oxygen affinity of Ni sites, and ultimately, enhance the production of valuable propenyl products *via* the synergistic effect of Pt and Ni. This work provides a strategy for maximizing Pt utilization and producing unsaturated chemicals from biomass under hydrogen-free conditions, advancing sustainable biorefining.

Introduction

Given with the ongoning concerns about global warming due to the overuse of fossil energy, more and more attention is being paid to the green, sustainable and renewable biomass resources. Lignocellulosic biomass containting cellulose (30~50%), hemicellulose (20~35%), and lignin (15~35%), represents the most abundant renewable carbon resource on the earth.[1-5] Efficient and

rational fractionation, depolymerization, and upgrading of lignocellulose for the production of high-value chemicals, fuels, and functional materials are of great importance.[6-9] Traditionally, fractionation of lignocellulose is a carbohydrate-oriented process, aiming to valorize (hemi)cellulose, whereas the valorization of lignin is ignored. While lignin, as one of the three major components of lignocellulose and the largest source of aromatics in nature (mainly composed of monolignols (*p*-coumaryl alcohol, coniferyl alcohol and sinapyl alcohol[10]), its valorization with (hemi)cellulose is paramount for the full utilization of lignocellulose.

The lignin-first biorefining has emerged as a pivotal strategy. This overarching strategy facilitates the active stabilization of reactive lignin intermediates during biomass fractionation to prevent condensation reactions. Broadly, the lignin-first encompasses various stabilization methods including reductive catalytic fractionation (RCF),[11,12] oxidative catalytic fractionation (OCF),[13,14] protection-group approaches.[15] Among these methods, RCF is widely used in biomass fractionation due to the high lignin phenolic monomers yield and good (hemi)cellulose retention.[16,17] The product selectivity of RCF is highly tunable based on the catalytic system,[18-24] typically favoring propyl-, propanol-, or propenyl-substituted phenols. Of these, the propenyl variants have garnered significant attention due to their unique double bonds, which enable functionalization into various high-value chemicals.[25] Samec et al. achieved 49 wt% yield of 2,6-dimethoxy-4-(prop-1-enyl)-phenol from birch wood using ethanol/water as solvent over 5 wt%Pd/C catalyst.[26] In addition, a choline chloride/ethylene glycol-based system was developed for hydrogen transfer reduction catalytic fractionation, yielding 36.2% propenyl phenols with 87.6% selectivity, but resulting in partial degradation of carbohydrates.[27] Besides, catalysts with low loading and high dispersion also demonstrate outstanding performance in RCF. Song and coworkers reported the atomic dispersed ruthenium catalyst (Ru/ZnO/C) and palladium catalyst

(Pd/ZnO/C) for acquiring propenyl-catechol (selectivity of 77%) and propenyl-phenols (selectivity of 62%), respectively.[28,29] Despite of the progress mentioned above, these processes were carried out at high temperature in organic solvent and consumed exogenous hydrogen (H_2 or alcohols).

Recently, our group developed an innovative self-hydrogen supplied catalytic fractionation (SCF) strategy by using structural hydrogens in hemicellulose as a hydrogen source. Over 2%Pt/$NiAl_2O_4$ catalyst, the fractionation and depolymerization of lignocellulose to phenolic monomers (yield of 46.6 wt%) was realized in water with cellulose intact.[30,31] Despite obvious advantages, such as operating without exogenous hydrogen, using only water as a solvent, and mild reaction conditions (140 °C), the SCF process still produces products with saturated side chains and requires a high Pt loading (2 wt%). Given that propenyl- or propanol-terminated products are more valuable, we questioned whether unsaturated side groups could be retained through the design of single-atom or single-atom alloy (SAA) catalysts. It well studied that SAA catalysts can offer unique active sites with high activity and improved sintering resistance,[32-34] so a tailored SAA catalyst for SCF process to enable unsaturated product formation under mild conditions was designed.

Herein, we reported a single-atom alloy (SAA) catalyst comprised of isolated Pt atoms stabilized by Ni atoms on $NiAl_2O_4$ spinel support for SCF of birch wood. The Pt_1Ni SAA catalyst was prepared by co-impregnation followed by H_2 reduction, achieved nearly theoretical maximum yield of phenolic monomers (50.9 wt%), corresponding to turnover numbers (TON) of 270.5 $mol_{phenols}\ mol_{Pt}^{-1}$. Surprisingly, propenyl side-chained syringol (selectivity 51.8%) co-existed with the propyl side-chained syringol at 140 °C for 12 h, the former has more functionality and can be used for bioactive molecules, pharmaceuticals, and materials synthesis.[35] The SCF over Pt_1Ni SAA

catalyst resulted in a cellulose-rich pulp with high glucan retention (90%) due to the mild reaction conditions. This catalyst also demonstrated good stability in recyclability experiments. Model compound catalytic experiments and density functional theory (DFT) calculations reveal that three pathways including C_α-OH deH, C_α-OH deOH-I, and C_α-OH deOH-II co-existed in lignin depolymerization. Pt_1Ni SAA catalyst could reduce the energy barrier for dehydroxylation, rendering it to outperform pure Pt catalyst in C_α-OH deOH. Moreover, C_α-OH deOH is superior to the C_α-OH deH pathway, thereby promoting the selectivity towards useful propenyl-ended products. During the preparation of this manuscript, we noted that Liao's work[36] reported a 79.6% selectivity for alkene-functionalized side-chain products, which was achieved under N_2 at 235 °C with methanol serving as solvent and hydrogen source *via* a different reaction pathway. Both studies efficiently produced unsaturated side-chain products, offering new strategies for the valorization of lignocellulose. The following work would be concentrated on designing more efficient catalyst to achieve high yield of alkene-functionalized side-chain products *via* SCF.

Results

Characterizations of the structure of the single-atom alloyed Pt_1Ni catalyst

0.2Pt5Ni/$NiAl_2O_4$ and 2Pt5Ni/$NiAl_2O_4$ catalysts were prepared by co-impregnation followed by H_2 reduction. As comparison, 2Pt/$NiAl_2O_4$ and 5Ni/$NiAl_2O_4$ catalysts were also prepared with the same method. The former (monometallic Pt loaded on spinel) was selected as a high-performance benchmark based on our previous work,[30] and the latter (monometallic Ni loaded on spinel) was chosen to determine the intrinsic baseline activity of pure Ni catalyst. The phase structures of these

catalysts were characterized by X-ray diffraction (Figure S1) and only the diffraction peaks (2θ = 19.1°, 31.4°, 37.0°, 45.0°, 59.7°, and 65.5°) corresponding to the (111), (220), (311), (400), (511), and (440) planes of $NiAl_2O_4$ (PDF #10-0339) were observed. No diffraction peaks of Pt and Ni were detected in all of the catalysts, probably due to the low loading or small particle size. N_2 sorption showed that the surface area changed less, all in the range of 61.6~93.0 $m^2 \cdot g^{-1}$. ICP-AES measurement gave the element composition of Pt (0.095, 0.97, and 1.7 wt%) and Ni (4.3, 4.7 wt%) in all samples and CO pulse chemisorption clearly revealed the good dispersion of Pt (58.5~95.5%). The physicochemical parameters of various samples were summarized in Table S1. The H_2-TPR profiles of various catalysts were shown in Figure S2. It shows that monometallic 5Ni/$NiAl_2O_4$ catalyst has a single reduction peak at 416 °C, attributed to the reduction of NiO species.[37] For 2Pt/$NiAl_2O_4$ catalyst, the reduction peak at 193 °C can be assigned to the reduction of PtO_x and the peak at 401 °C is related to the co-reduction of PtO_x and NiO_x species in $NiAl_2O_4$.[38] For PtNi/$NiAl_2O_4$ catalysts with two different Pt loadings, the reduction peaks of NiO species moved to lower temperature because the doping of Pt makes it easier for NiO to be reduced. In addition, the reduction peaks of PtO_x were not detected for the 0.2Pt5Ni catalyst. This is likely due to the low loading of Pt (0.2 wt%), which falls below the detection limit of the TCD. Specifically, the H_2-TPR profiles reveal that Pt facilitates NiO reduction via hydrogen spillover, where dissociated hydrogen on Pt reduces adjacent NiO species. This confirms the structural intimacy of Pt and Ni, supporting potential alloy formation and enhancing overall catalyst reducibility.

To identify the position of Pt in 0.2Pt5Ni/$NiAl_2O_4$ catalyst, aberration-correction high-angle annular dark-field scanning transmission electron microscopy (HAADF–STEM) and energy-

dispersive spectroscopy (EDS) elemental mapping were conducted. The EDS elemental mappings illustrate a high dispersion and close contact of Pt on Ni nanoparticles (Figure 1a, b). HAADF-STEM image displays the lattice spacing of ~0.181 nm in 0.2Pt5Ni catalyst (Figure 1c). This lattice spacing corresponds to that of Ni (200) plane, but larger than that of pure Ni (200) plane of 0.176 nm, indicating the occurrence of lattice expansion. Enlarged STEM image shows that number of atom-sized bright spots (highlighted by the red cycles) distributed on the surface of Ni NPs and these atoms are attributed to individual Pt atoms, Meanwhile, no Pt clusters or nanoparticles were observed (Figure 1d), which demonstrated the formation of Pt_1Ni single-atom alloy. In comparison, the HAADF-STEM image of 2Pt5Ni/$NiAl_2O_4$ catalyst was also presented (Figure S3) and both Pt single atoms and Pt clusters are detected on Ni NPs, indicating an aggregation of Pt atoms due to the increase in loading. Meanwhile, the 2 wt% Pt/$NiAl_2O_4$ was synthesized as a control sample, in which Pt clusters were uniformly distributed on the surface of $NiAl_2O_4$ support with an average particle size of 1.4 nm (Figure S4).

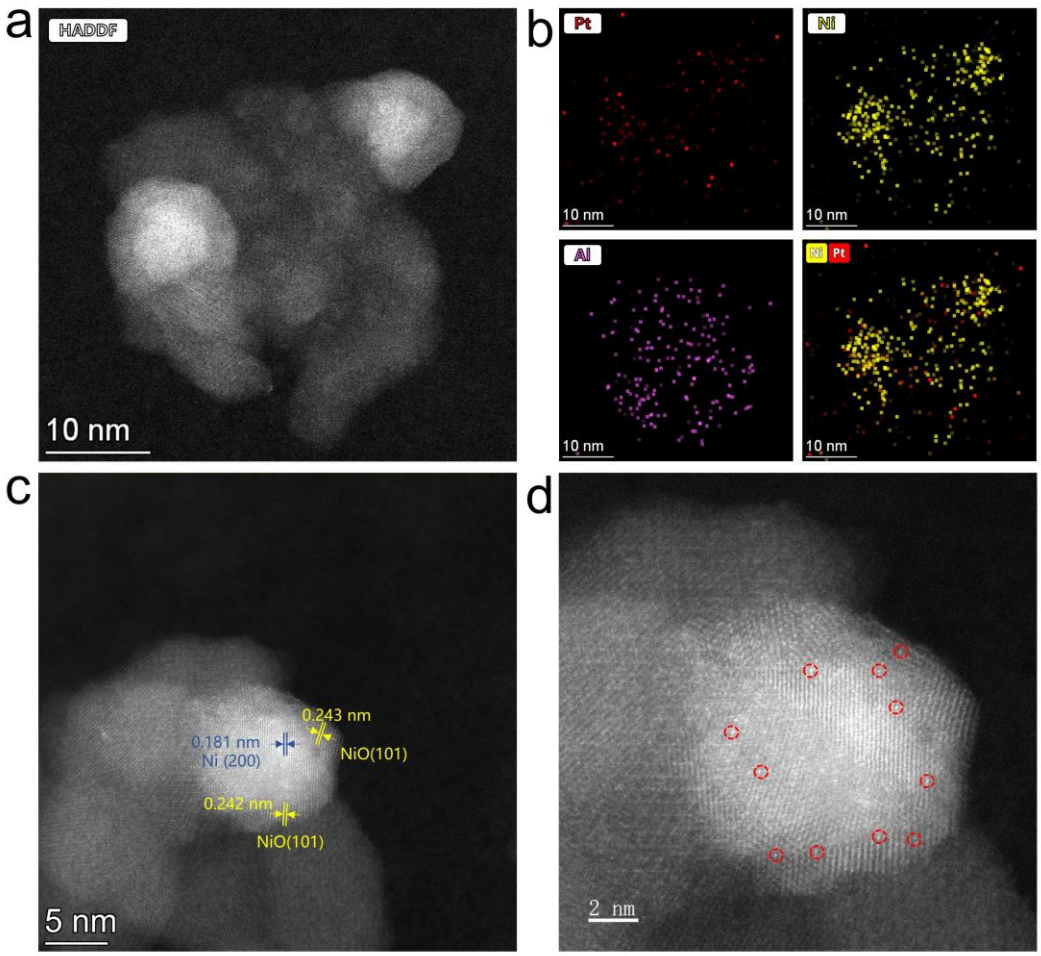

Figure 1. Electron microscopy characterization of 0.2Pt5Ni catalyst. (a) HAADF-STEM image, (b) corresponding EDS-mapping images of Pt, Ni, Al, and O elements, (c) AC- HAADF-STEM image with corresponding lattice fringe, (d) enlarged STEM image of c.

To further explore the structural details of 0.2Pt5Ni catalyst, in situ DRIFTS spectra of CO adsorption was recorded. As comparison, $2Pt/NiAl_2O_4$, $5Ni/NiAl_2O_4$ and $2Pt5Ni/NiAl_2O_4$ catalysts were also investigated (Figure 2a). CO adsorption on $2Pt/NiAl_2O_4$ catalyst generates dominant peak at 2066 cm^{-1}, which is assigned to the linearly absorbed CO at Pt clusters.[38,39] For monometallic $5Ni/NiAl_2O_4$ catalysts, almost no CO adsorption is detected. In the case of 0.2Pt5Ni

catalyst, the observed peak at 2034 cm^{-1} is assigned to linearly absorbed CO at Pt single atom, the red shift of the linearly absorbed CO peak indicates an enhanced metallicity of Pt species in PtNi catalyst. This would come from the electron transfer from Ni to Pt, which increases the d-π electron feedback from Pt to CO 2π* antibonding orbital.[40,41] Interestingly, a broad peak at 1835 cm^{-1} is also observed, which is assigned to bridged-bonded CO at contiguous Ni atoms. For 2Pt5Ni catalyst, in addition to the main peak at 2066 cm^{-1}, an obvious shoulder centered at ~2034 cm^{-1} is observed, indicating that the catalyst contains a mixture of Pt single atom and Pt cluster, consistent with the STEM observations.

To further study the electronic and geometric structure of PtNi catalysts, the Pt L_3-edge X-ray absorption near-edge (XANES) spectra were conducted with Pt foil and PtO_2 as reference. As shown in Figure 2b, the 0.2Pt5Ni and 2Pt5Ni catalysts have lower intensity of "white line" than that of 2Pt/$NiAl_2O_4$ catalyst, indicating a more reduced state of Pt species of PtNi catalyst, in accordance with CO-DRIFTS results. The Fourier transforms of the extended X-ray absorption fine spectrum (EXAFS) in the R space was performed to investigate the detailed coordination structure of Pt (Figure 2c). The 0.2Pt5Ni catalyst exhibits a unique peak located at ~2.1 Å, which can be assigned to the Pt-Ni coordination.[41,42] The EXAFS data-fitting results (Table S2 and Figure S5) show that the coordination number (CN) of Pt-Ni path is 6.6, while Pt-Pt coordination is absent in 0.2Pt5Ni catalyst. This verifies that predominant Pt atoms are atomically dispersed and surrounded by Ni to form single-atom alloy. For 2Pt5Ni and 2Pt/$NiAl_2O_4$ catalysts, the Pt-Pt coordination number are 2.5 and 3.4, respectively, indicating the Pt atoms aggregate gradually upon increasing Pt loading. The k^2-weighted wavelet transforms (WT) for the Pt L_3-edge XAFS

signals were further employed to study coordination environment of Pt species. As shown in Figure 2d~f, the WT contour plots of 0.2Pt5Ni catalyst display only one Pt-Ni coordination intensity maximum at 2.1 Å, 7.2 $Å^{-1}$, without other scattering paths compared with the WT plots of Pt foil and PtO_2, demonstrating the formation of SAA. In brief, the results of AC-HAADF-STEM, CO-DRIFTS as well as XAFS experiments confirm the successful preparation of Pt_1Ni SAA catalyst.

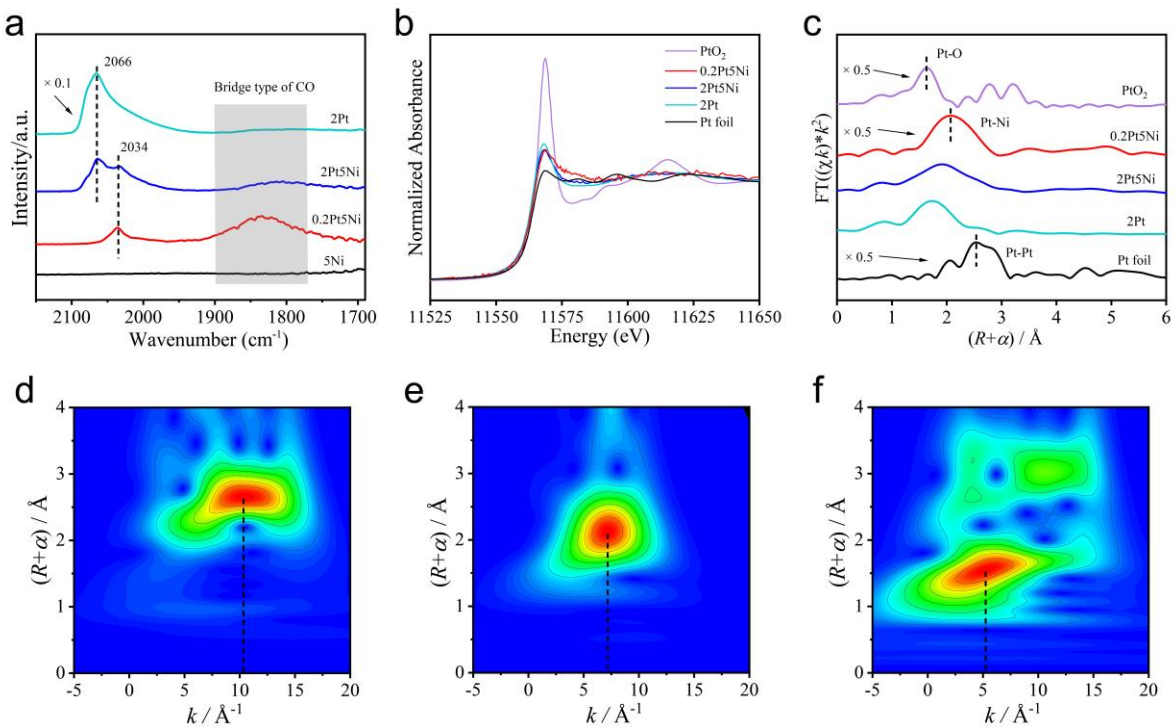

Figure 2. Fine-structure characterizations of PtNi catalysts. (a) In situ CO-DRIFTS spectra of $2Pt/NiAl_2O_4$, $5Ni/NiAl_2O_4$, 2Pt5Ni, and 0.2Pt5Ni catalysts. (b) Pt L_3-edge XANES spectra and (c) EXAFS Fourier–transform spectra of various samples. k^2-weighted wavelet transforms for the Pt L_3-edge XAFS signals of (d) Pt foil, (e) 0.2Pt5Ni sample, and (f) PtO_2 based on Morlet wavelets (The data are not phase-corrected).

Performance of $PtNi/NiAl_2O_4$ in the self-hydrogen supplied catalytic fractionation (SCF)

Birch wood, a typical hardwood substrate containing 43.6 wt% of cellulose, 18.4 wt% of hemicellulose and 20.1 wt% of lignin, was initially used for SCF. The reaction was performed at 140 °C and 1 atm N_2 in water with the substrate to catalyst ratio at 0.5/0.2. Firstly, we evaluated the performance of pristine $NiAl_2O_4$ support and found that almost no product was detected, indicating that the pure carrier is basically inactive (Table 1). The $5Ni/NiAl_2O_4$ catalyst exhibited no measurable activity, which is consistent with the finding that its surface is primarily composed of NiO species, confirming the inactivity of NiO in this reaction. In contrast to monometallic catalysts, all PtNi catalysts showed significantly enhanced catalytic activity (Table 1). As shown in Table 1, 0.2Pt5Ni catalyst achieved the yield of phenolic monomers (38.6 wt%) with 51.8% selectivity to 4-propenyl guaiacol/syringol (Pe-G/S) at 140 °C for 12 h (Figure S6), corresponding to TON as 216.6 $mol_{phenols}\ mol_{Pt}^{-1}$ (The TON was calculated based on the total number of moles of Pt in 0.2Pt5Ni catalyst). When the reaction time was prolonged to 24 h at 140 °C, the phenolic monomers yield further increased to 50.9 wt%, approaching the theoretical maximum yield of phenolic monomers,[14] with the TON reached 270.5 $mol_{phenols}\ mol_{Pt}^{-1}$, larger than most results of reported catalytic systems (Figure S7), indicating the superiority of single atom alloyed Pt_1Ni catalyst. In contrast, the $0.2Pt/NiAl_2O_4$ catalyst (Table 1, entry 7) was inert, indicating that Pt-Ni interactions are crucial for the SCF process (Tables S3 and S4). This conclusion was further supported by a control experiment using a mechanical mixture of the monometallic catalysts (Table 1, entry 8). Collectively, the characterization and control experiments indicated that the high activity of the Pt_1Ni catalyst originates from the single-atom alloy structure, which effectively stabilizes metallic Ni species. Interestingly, among all monomers obtained over Pt_1Ni catalyst, 4-

propenyl syringol (Pe-S, 19.9 wt%) was always co-existed with 4-propyl syringol (Pr-S, 23.5 wt%) as major products, with 4-propenyl guaiacol (Pe-G, 0.9 wt%), 4-propyl guaiacol (Pr-G, 3.2 wt%) and 4-ethyl syringol (Er-S, 3.4 wt%) as the minors (corresponding birch lignin monomers concentrations are shown in (Table S5). The structural features and molecular weight distribution of the obtained lignin oil were characterized by 2D HSQC NMR and GPC, respectively (Figures S8 and S9). In addition, the glucan in the pulp showed the good retention (90 %) based on the 43.6 wt% of cellulose in the birch and the pulp also showed the 70 % of the crystallinity index (CrI) (Figure S10). 2Pt and 2Pt5Ni catalyst also obtained good phenolic monomers yield of 36.2 wt% and 48.5 wt%, respectively. But almost no 4-propenyl guaiacol(syringol) were detected in the obtained products, and the TONs were calculated as 34.9 and 30.5 $mol_{phenols}$ mol_{Pt}^{-1}, respectively, which were far lower than that from 0.2Pt5Ni catalyst, the latter indeed realize the maximization of Pt utilization efficiency.

Furthermore, we conducted SCF of birch wood over different PtNi catalysts based on same Pt usage (by adjusting catalyst dosage, Table S6), and found only 2.2 wt% phenolic monomers yield were achieved over 2Pt5Ni catalyst, but 0.2Pt5Ni catalyst still remain high performance (38.6 wt% phenolic monomers yield), further confirming the high efficiency of 0.2Pt5Ni alloy catalyst. To better elucidate the unique role of the $NiAl_2O_4$ support in the reaction, we synthesized a 0.2Pt5Ni/Al_2O_3 catalyst using Al_2O_3 as the support for comparison. The results showed that $NiAl_2O_4$ support exhibited superior performance in the selective depolymerization of lignin. This is driven by abundant oxygen vacancies, promoted hydrogen spillover, and robust metal-support interactions (Tables S7 and S8, Figure S11-S13). Notably, the superior hydrothermal stability of

the $NiAl_2O_4$ support relative to Al_2O_3 support plays an indispensable role in this process. In addition, various oxygen affinity transition metals (e.g., Nb, Mo, W) were also screened for SCF of birch wood (Table S9). Results indicate that the 0.2Pt5W and 0.2Pt5Mo catalysts yield only 14.7% and 8.9% phenolic monomers, respectively. Notably, no phenolic monomers were detected on 0.2Pt5Nb catalyst. The reason for the above results may be that Nb, Mo, and W are difficult to reduce and cannot form alloy structures with metal Pt, further demonstrating the crucial role of Ni in self-hydrogen supplied fractionation.

Table 1. SCF of birch wood over various PtNi catalysts.[a]

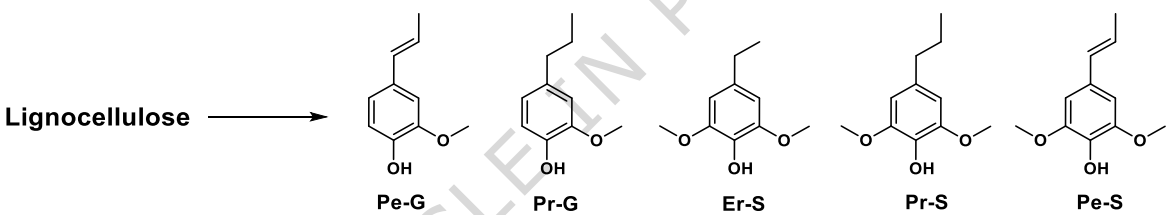

Entry	Sample	Phenolic monomers yield (wt%)					Sel. to Pe-G/S (%)	Total (wt%)	TON
		Pe-G	Pr-G	Er-S	Pr-S	Pe-S			
1	0.2Pt5Ni	0.5	1.2	2.4	15.0	19.5	51.8	38.6	216.6
2	0.2Pt5Ni[b]	0.9	3.2	3.4	23.5	19.9	40.9	50.9	270.5
3	2Pt5Ni	-	2.1	16.6	28.4	1.4	2.9	48.5	30.5
4	2Pt	-	2.0	6.1	25.3	2.8	7.7	36.2	34.9
5	5Ni	-	-	-	-	-	-	-	-
6	$NiAl_2O_4$	-	-	-	-	-	-	-	-
7	0.2Pt	-	-	-	-	-	-	-	-
8	0.2Pt+5Ni[c]	-	0.1	0.2	1.5	3.3	-	5.1	-

[a] Reaction conditions: birch wood (0.5 g), catalyst (0.2 g), H_2O (10 mL), N_2 1 atm, 140 °C, 12 h.

[b] Reaction time: 24 h.

[c] The reaction was carried out with 0.2Pt/$NiAl_2O_4$ (0.1 g) and 5Ni/$NiAl_2O_4$ (0.1 g).

Above results showed that over 0.2Pt5Ni catalyst, 4-propenyl syringol (Pe-S) and 4-propyl syringol (Pr-S) are all co-existed as main products, which was different from traditional RCF and SCF strategy over 2%Pt/$NiAl_2O_4$ catalyst. In the latter processes, 4-propenyl syringol was less detected although it was more useful due to the existence of the active C=C bond in C_3 tail chain. In order to investigate the reaction pathway, the reaction time profile of SCF was conducted and the results were presented in Figure 3. It is shown that in the first 16 h, the yields of Pr-S and Pe-S both increased with the prolonging of time, indicating probably two reaction pathway co-existed, different from that over 2%Pt/$NiAl_2O_4$ as we reported before (Figure S14).[30] With the further extension of the reaction time to 24 h, the yield of Pe-S decreased and the yield of Pr-S further increased. A plausible explanation is that as the reaction proceeds, most of the lignin is removed (delignification up to 94%) and no new monomers are produced, hence the Pe-S is gradually hydrogenated to Pr-S in the presence of hydrogen. The hydrogen source origins from hemicellulose as we described recently.[41]

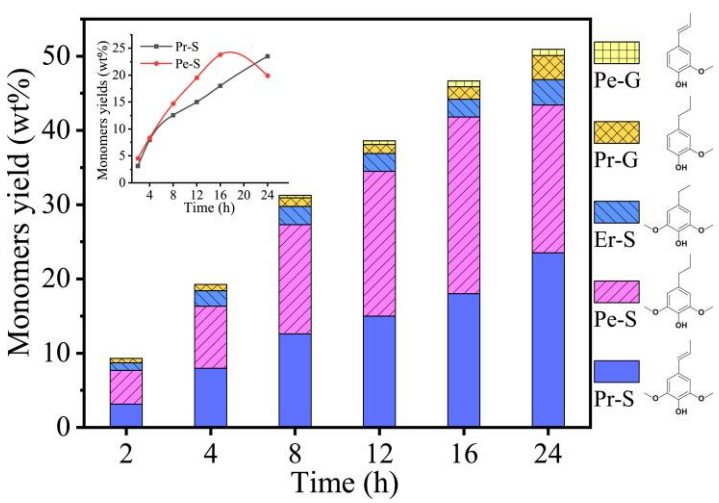

Figure 3. Time profile of birch SCF reaction over 0.2Pt5Ni catalyst.

Furthermore, the reusability of the catalyst was investigated. The total phenolic monomers yield of 30.5 wt% was achieved with 47.5% selectivity of 4-propenyl guaiacol/syringol (Pe-G/S) at 140 °C for 12 h in the third run (Table S10), a slight decrease yield compared to the first run, indicating the catalyst has good stability in SCF process. The above results imply 0.2Pt5Ni catalyst has excellent activity for SCF of birch wood, and can be further extended to other biomass (pine wood and wheat straw), the total phenolic monomers yield of 28.5 wt% with 26% selectivity of 4-propenyl guaiacol/syringol (Pe-G/S) and 10.8 wt% with 40.7% selectivity of 4-propenyl guaiacol/syringol (Pe-G/S) for pine wood and wheat straw, respectively (Table S11). In addition, the obtained monophenols (lignin oil) could further convert to 4-alkylphenols by demethoxylation in the absence of exogenous hydrogen over RuNi/$NiAl_2O_4$ catalyst.[43] Under optimized conditions, 20.5 wt % yield of 4-alkylphenols could be acquired from birch lignin oil (Figure S15).

Intrinsic catalytic activity and reaction pathways

To further investigate the possible reaction pathways in the SCF process, typical β-O-4 lignin model compound, syringyl-glycerol-β-guaiacyl ether (SG, **1a**), was used to evaluated the reaction pathways over 0.2Pt5Ni/$NiAl_2O_4$ and 2Pt/$NiAl_2O_4$ catalysts. To be consistent with the reaction conditions of birch wood, we then added xylan as hydrogen source in the transformation of lignin model compounds. As shown in Table 2, when **1a** was used as the reaction substrate over the 0.2Pt5Ni catalyst for 1 hour, the dimeric intermediates, 1-(4-hydroxy-3,5-dimethoxyphenyl)-3-hydroxy-2-(2-methoxyphenoxy)-1-propanone (**2a**), 4-(3-hydroxy-2-(2-methoxyphenoxy)propyl)-2,6-dimethoxyphenol (**3a**), and 4-(3-Hydroxy-2-(2-methoxy-phenoxy)-propenyl)-2,6-

dimethoxy-phenol (**4a**) were detected with yields of 2 wt%, 0.8 wt%, and 11 wt%, respectively, indicating there are three potential reaction pathways and the main reaction pathway is the dehydroxylation of C_α-OH and formation of C_α=C_β double bond. Importantly, the unsaturated C=C products, derived from the cleavage of **4a**, sinapyl alcohol (**6a**) and its dehydroxylation product Pe-S (**11a**), were detected with yields of 6.1 wt% and 19.5 wt%, respectively. This is consistent with the results of the SCF reaction of birch wood, which primarily yields 4-propenyl products. Additionally, the phenolic monomers with side-chain saturated and oxygen-containing (**7a, 8a, 9a, 10a**, and **12a**) were also detected with yields of 8 wt%, 0.4 wt%, 1.2 wt%, 0.7 wt%, and 1.3 wt%, respectively. With the reaction time extended to 4 hours, the unsaturated C=C products gradually decreased due to hydrogenation and lead to over-reaction, with the yields of **8a** and **10a** increased. In addition, we conducted control experiments on model compound SG using different types of hydrogen sources, such as xylan, isopropanol, and H_2. The consistent reaction pathway was observed, demonstrating that the formation of propenyl-substituted phenolic products is primarily determined by intrinsic catalytic properties rather than hydrogen sources (Table S12).

Table 2. Reaction pathway of lignin model compound SG at different reaction times.

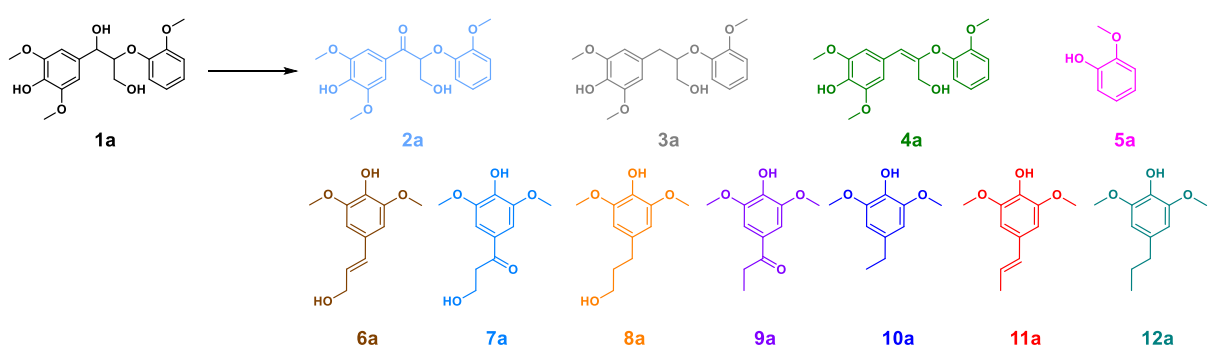

Entry	Catalysts	Time (h)	Conv. (%)	Yield (wt%)										
				2a	3a	4a	5a	6a	7a	8a	9a	10a	11a	12a
1	0.2Pt5Ni	1	100.0	2.0	0.8	11.0	39.0	6.1	8.0	0.4	1.2	0.7	19.5	1.3
2	0.2Pt5Ni	4	100.0	4.7	0.3	0.2	43.3	0.3	0.3	12.0	3.9	11.7	6.2	6.7
3	2Pt	1	100.0	9.2	0.4	-	40.3	-	17.3	5.1	6.7	5.2	-	4.0
4	2Pt	4	100.0	3.1	0.5	-	44.2	-	1.0	5.7	11.0	8.7	-	16.4

Reaction Conditions: Xylan (0.05 g), Substrate (0.1 g), catalyst (0.1 g), H_2O (10 mL), N_2 1 atm, 140 °C.

In contrast, no dimer intermediate **4a** and the corresponding monomers **6a** and **11a** were produced over the 2Pt catalyst within 1 hour of reaction, while a large amount of monomer **7a** (17.3%) was produced, indicating a distinct reaction pathway compared to the 0.2Pt5Ni catalyst. The same pattern was also observed in experiments using hydroxyphenyl-glycerol-β-guaiacyl ether (HG) and guaiacyl-glycerol-β-guaiacyl ether (GG) as the substrate (Tables S13 and S14), suggesting that three reaction pathways co-exist over the 0.2Pt5Ni catalyst, while the 2Pt catalyst has a relatively single reaction pathway (C_α-OH dehydrogenation) and is unable to produce the unsaturated dimer intermediates **4a**, **4b**, and **4c**. This might be due to the stronger hydrogen generation and hydrogen migration capabilities of the 2Pt catalyst compared to the 0.2Pt5Ni catalyst (Figure S16).

DFT calculations

To gain a deeper understanding of the reaction mechanism and pathways, the DFT calculations were performed to investigate the mechanism of SG hydrogenation on the exposed (100) facet of

Pt and Pt_1Ni. Figure S17 shows the SG could preferentially chemisorb on the $Pt_1Ni(100)$ and Pt(100) surfaces *via* the flat-lying configuration, at which both benzene rings in SG were bonded to the surfaces. The higher binding strength between benzene rings and Pt(100) indicates the stronger carbophilicity of platinum. The conversion of chemisorbed SG can potentially start with the dehydrogenation of $(C_\alpha)OH$, the hydrogenolysis of C_α-OH, the ether C-O bond cleavage, or the dehydrogenation of C_α-H. Among these steps, the lowest free energy barrier step is the hydrogenolysis of C_α-OH over $Pt_1Ni(100)$, while it is the dehydrogenation of $(C_\alpha)OH$ over Pt(100) (Figure S18). This indicates that the hydrogenolysis of C_α-OH would preferentially occur over $Pt_1Ni(100)$, while the dehydrogenation of $(C_\alpha)OH$ would be more favorable over Pt(100). This could be attributed to the higher oxophilicity of nickel compared to platinum.[44] The Crystal Orbital Hamilton Populations (COHP) analysis (Figure S19) confirms that the strong adsorption of oxygen atoms by Ni sites on the Pt_1Ni (100) surface weakens the C_α-OH bond compared to Pt(100), resulting in a 0.04 Å elongation and thereby facilitating C_α-OH bond cleavage. It indicates that Pt_1Ni (100) might be more favorable to produce the intermediates with unsaturated C=C bond, such as **4a**, while Pt (100) is more favorable to produce the intermediates with carbonyl group, such as **2a**, at the initial stage of the SG hydrogenation. This aligns with the observed differences in product distribution (Table 2) and the reaction pathways proposed based on experimental observations.

To distinguish how these initial steps govern subsequent reactivity, we conducted a further mechanistic study of the reaction pathways, commencing with the hydrogenolysis of C_α-OH and the dehydrogenation of C_α-OH over the two catalysts. The corresponding pathways were labelled

as Cα-OH deOH towards the production of **8a**, **6a**, and **11a**, and Cα-OH deH towards the production of **7a**, respectively. In the Cα-OH deH pathway (Figure S20), each elementary step exhibits a higher energy barrier on Pt_1Ni (100) than Pt (100). Specifically, the water-mediated dehydrogenation of the Cα-H for the production of **2a** encounters a free energy barrier of 1.11 eV (TS2-1) on Pt_1Ni(100), while the subsequent ether C-O bond cleavage requires an even higher barrier of 1.51 eV (TS3-1). In contrast, the higher carbophilicity of Pt sites lead to the reduced energy barriers for the dehydrogenation of Cα-H (TS2-1', 0.77 eV) and the ether C-O bond breaking (TS3-1', 0.80 eV) over Pt(100). These results imply higher selectivity towards **7a** over Pt(100) compared to Pt_1Ni(100), which aligns well with the product distribution listed in Table 2. The Cα-OH deOH branches into two pathways after the dehydroxylation: (I) hydrogenation of Cα-H to produce **3a** first and (II) dehydrogenation of Cβ-H to produce **4a** first. In the Cα-OH deOH-I pathway (Figure S21), the least stable TS was found in the hydrogenolysis of Cα-OH (TS1-2') on Pt(100), which is less stable than the rate-determining TS of the ester C-O bond breaking (TS3-2, 0.73 eV) on Pt_1Ni (100). This would limit the **8a** production on Pt(100). Figure S22 shows that the energy barriers of most steps on Pt_1Ni(100) are lower than those on Pt(100) in the Cα-OH deOH-II pathway. The TS of the hydrogenolysis of Cα-OH on Pt(100) (TS1-2') is still the most unstable TS, which is less stable than the rate-determining TS for the ester C-O bond breaking on Pt_1Ni(100) (TS3-3). Moreover, the barrier of the ester C-O bond breaking on Pt_1Ni(100) (G_a = 1.43 eV) is lower that on Pt(100) (G_a = 1.46 eV). These suggest that Pt_1Ni(100) would surpass Pt(100) in the Cα-OH deOH-I and Cα-OH deOH-II pathways, while Pt(100) would be superior to Pt_1Ni(100) in the Cα-OH deH pathway. Hence, the oxophilicity of nickel could facilitate the production of propenyl

side-chained compounds on $Pt_1Ni(100)$.

In Figure 4, we energetically compared the three pathways to understand the selectivity of SG hydrogenation on the $Pt_1Ni(100)$ surface. Notably, the rate-determining step in each pathway is the ether C-O bond cleavage. It needs to overcome the free energy barrier of 1.51 eV in C_α-OH deH pathway, corresponding to the step from IM2-1 to IM3-1. Similarly, the ether C-O bond breaking step of IM2-2 to IM3-2 is the most difficult step in the C_α-OH deOH-I pathway, requiring an energy input of 1.48 eV. In the C_α-OH deOH-II pathway, the ether C-O bond breaking of IM2-3 to IM3-3 requires the lowest energy input of 1.43 eV among the three pathways. The lower energy barrier of the rate-determining C-O ether bond breaking indicates that the C_α-OH deOH-II would be superior to the C_α-OH deOH-I and C_α-OH deH pathways, indicating a higher yield of **6a** and **11a** for SG hydrogenation. It is also in good agreement with our experimental observation. Noteworthily, the **6a** produced in C_α-OH deOH-II pathway at the metal Pt_1Ni site is an enol ether intermediate, which is a crucial intermediate in lignin depolymerization. The C_β-O bond of this intermediate could be further cleaved to produce propenyl-ended products.

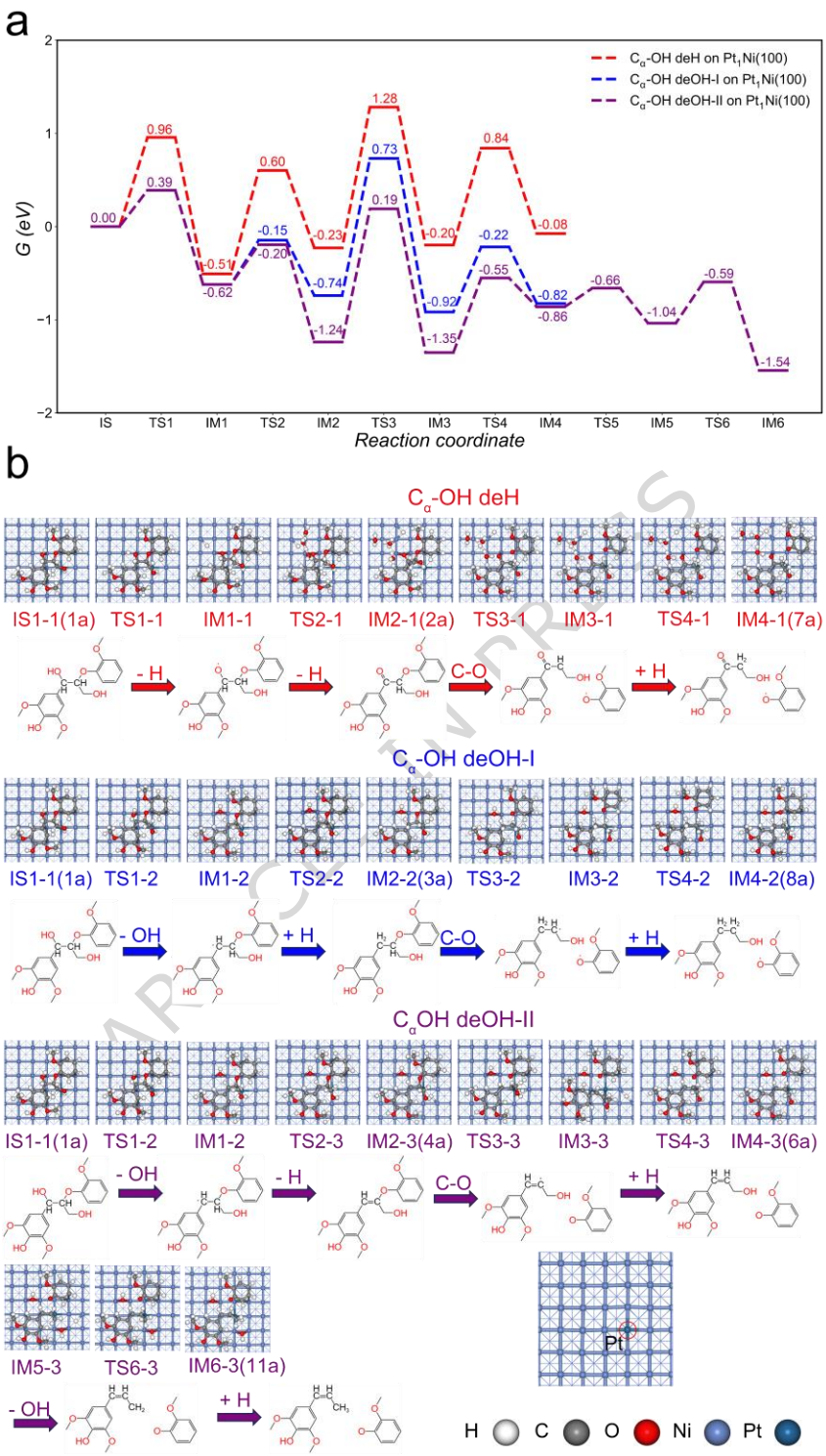

Figure 4. The comparative diagram of the reaction pathways. (a) energy profiles for Cα-OH deH, Cα-OH deOH-I, and Cα-OH deOH-II on $Pt_1Ni(100)$. (b) corresponding the molecular structure diagram. The Pt atoms in $Pt_1Ni(100)$ have been circled in red in the last figure.

Based on the results of model compound catalytic experiments and DFT calculations, we provide a possible mechanism of lignin depolymerization in this work (Figure 5). Three pathways (C_α-OH deH, C_α-OH deOH-I, and C_α-OH deOH-II) co-existed in lignin depolymerization. (i) C_α-OH deH: dehydrogenation of the C_α-OH in β-O-4 units to ketone intermediates. Then, the C_β-O bond of the intermediate will cleave to monomers, followed by hydrogenolysis and hydrogenation process to obtain 4-propyl-syringol (guaiacol). (ii) C_α-OH deOH-I: hydrogenolysis of C_α-OH in β-O-4 units, then cleavage of C_β-O bond, further to obtain 4-propyl-syringol (guaiacol). (iii) C_α-OH deOH-II: hydrogenolysis of C_α-OH and dehydrogenation of C_β-H to enol ether intermediate, then cleavage of C_β-O bond, further to obtain 4-propenyl-syringol (guaiacol). In addition, acid formed in biomass depolymerization may also be involved in the reaction, which also promotes the C_α-OH deOH-II pathway and therefore produces more propenyl-ended products.

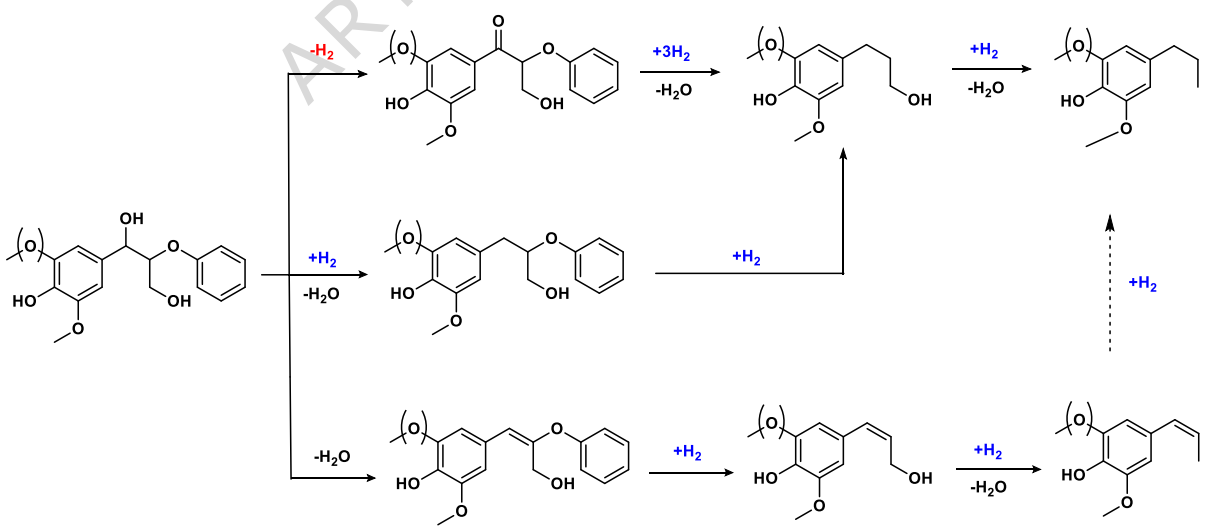

Figure 5. Proposed mechanism of lignin depolymerization in SCF.

Discussion

In summary, we developed an innovative Pt_1Ni single-atom alloy (SAA) catalyst for hydrogen-free catalytic fractionation of lignocellulose via self-hydrogen supplied catalytic fractionation (SCF) strategy. The single-atom alloy structure was unambiguously confirmed by multiple characterization techniques, including AC-HAADF-STEM, in situ CO-DRIFTS, and EXAFS. Under mild conditions (140 °C, 24 h), the catalyst achieved a near-theoretical yield of phenolic monomers (50.9 wt%), predominantly propyl/propenyl-substituted syringol derivatives, while preserving cellulose integrity. The system exhibited a high turnover number (TON) of 270.5 $mol_{phenols} \cdot mol_{Pt}^{-1}$ and demonstrated good recyclability under operational conditions. Model compound catalytic experiments and density functional theory (DFT) calculations reveal the coexistence of three pathways (C_α-OH deH, C_α-OH deOH-I, and C_α-OH deOH-II) based on the different dimeric intermediates in lignin depolymerization and Pt_1Ni SAA catalyst is superior to pure Pt catalyst for the Cα-OH deOH-I and Cα-OH deOH-II, while Pt(100) would be superior to Pt_1Ni(100) for the Cα-OH deH. Over Pt_1Ni SAA catalyst, the C_α-OH deOH II is easier due to the oxygen affinity of Ni sites and forms C_α=C_β double, leading to propenyl products formation through enol ether intermediate. In addition, compared to pure Pt catalyst, Pt_1Ni SAA catalyst can lower the energy barrier for breaking C-O bonds, which is rate-determining step in three pathways. This work provides significant advances in the design of high-performance single-atom alloy catalysts for sustainable lignin depolymerization and contributes to the holistic valorization of lignocellulosic biomass in the context of biorefinery.

Methods

Catalyst preparation

$NiAl_2O_4$ spinel was synthesized by a coprecipitation method at a Ni/Al mole ratio of 1:2.[38, 45] A typical procedure is as follows: 40 mmol nickel nitrate hexahydrate and 80 mmol aluminum nitrate nonahydrate were dissolved in 200 ml of ultrapure water under vigorous stirring at room temperature. Aqueous ammonia (25-28 wt%) was added dropwise to the above solution until the pH reached 8 to obtained precipitates. Then, the formed precipitates were filtered and washed with deionized water until the pH of the filtrate reached 7. Finally, the filter cake was dried at 100 °C for 24 h, followed by calcination at 800 °C for 8 h under Ar atmosphere. xPtyNi/$NiAl_2O_4$ (where x, y represents the loading weight of Pt and Ni, respectively) was prepared by the co-incipient wetness impregnation method with appropriate amounts of aqueous solution of chloroplatinic acid (H_2PtCl_6) and $NiCl_2 \cdot 6H_2O$, respectively. The obtained samples were dried at 60 °C for 12 h and then reduced in a 10% H_2/Ar flow at 400 °C for 3 h. To make the Tables/Figures look more concise, we use xPtyNi represent xPtyNi/$NiAl_2O_4$ catalysts.

Catalyst characterizations

The powder X-ray diffraction (XRD) patterns were recorded on a Rigaku D/max-2550VB/PC diffractometer by using Cu Kα radiation (λ=0.15406 nm). Nitrogen adsorption/desorption isotherms of the catalysts were measured on a Micromeritics ASAP 2020M sorption analyser at 77K. The Brunauer-Emmett-Teller (BET) method was used to calculate the surface area. Aberration-corrected-HAADF-STEM images and EDS mappings were collected at 300 kV on a ThermoFisher Scientific Spectra 300 scanning transmission electron microscope equipped with a

Super-X EDS detector system. Inductively coupled plasma atomic emission spectrometry (ICP-AES) was used to determine the Pt/Ni loading content by using an Agilent 725ES.

H_2 temperature-programmed reduction (H_2-TPR) experiments were conducted on VDSorb-91i automatic chemisorption system. Typically, 0.1 g of catalyst was injected into the quartz sample tube. Before each run, the catalyst sample was in situ pretreated with Ar at 150 °C for 1 h and cooled down to ambient temperature. Then, the samples were heated to 700 ºC with a 10 °C min^{-1} ramp in 10% H_2/Ar flow.

CO pluse chemisorption tests were operated on VDSorb-91i automatic chemisorption system. Typically, 0.1 g of catalyst was injected into the quartz sample tube. Before each run, the catalyst sample was in situ reduced in flowing 10% H_2/Ar at 400 °C for 1 h and cooled down to ambient temperature with He. The CO pluse chemisorption results were calculated on the basis of the peak areas of the CO pulse injection (220 μL per pulse, 50% CO/He), which were monitored by a TCD detector (45 °C, 80 mA).

In situ diffuse reflectance infrared Fourier transform (DRIFTS) of CO adsorption was collected with a Nicolet iS50 FTIR spectrometer equipped with an MCT/A detector. Firstly, putting around 20 mg of catalyst into the chamber, the catalyst was in situ reduced in flowing 10% H_2/Ar at 400 °C for 1 h and decreased to 30 °C, followed by collecting the background spectrum. 1% CO/Ar was then introduced into the chamber for 30 min. Next, the chamber was purged with Ar for another 30 min and the adsorption spectra of CO was recorded. All spectra were collected after subtracting the background with a resolution of 4 cm^{-1} and an accumulation of 32 scans.

XAS measurements were conducted at the Canadian Light Source for the Pt L_3-edge on the Hard X-ray Micro-Analysis Beamline (HXMA). beamline. Pt foil was used for energy calibration and both fluorescence and transmission yields were recorded. fluorescence spectra were reported for samples with low Pt loading. Data analysis was performed using a standardized IFEFFIT package (including Athena and Artemis software).[46]

Catalytic reactions

In a typical SCF reaction, 0.5 g birch wood, 0.2 g xPtyNi/$NiAl_2O_4$ catalyst and 10 mL H_2O were put into the 50 mL stainless-steel autoclave reactor. The reactor was sealed and purged with N_2 at room temperature, then heated to different temperatures and kept for a certain time at a magnetic stirring speed of 700 rpm. At the end of the reaction, it was cooled down to room temperature in ice water. The soluble fraction and residue were subsequently separated by centrifugation.

Lignin-derived Products Analyses

After SCF reaction, the liquid phase was extracted by ethyl acetate and analyzed by GC-MS (Agilent 7890A) and quantitatively analyzed by GC (Agilent 7890B) with a flame ionization detector, both quipped with HP-5 capillary columns. Tridecane was used as an internal standard for the quantification of the liquid products. Nitrogen was employed as a carrier gas, and the following operating conditions were adopted: injection temperature 250 °C, column temperature program: 50 °C (hold time 3 min), 10 °C min^{-1} to 250 °C (hold time 5 min), detection temperature of 280 °C. Response factors for the different products were determined by calibration with commercial standards or through calculations based on the effective carbon number (ECN) theory.[47] All experiments were performed at least three times. The phenolic monomers yields were

calculated based on the Klason lignin weight, calculating formula as shown below:

$$\text{Phenolic monomers (wt\%)} = \frac{\text{Mass (total monomers)}}{\text{Mass (Klason lignin)}} \times 100\% \quad (1)$$

$$\text{Mole yields of monomers (\%)} = \frac{\text{Mole (total monomers)}}{\text{Mole (all monomers in lignin)}} \times 100\% \quad (2)$$

The mass of lignin in biomass was measured by Klason method and the mole of monomers in lignin was measured by NBO method.[15]

Computational details

All the calculations were performed in the framework of periodic density functional theory (DFT) using the Perdew-Burke-Ernzerhof (PBE) functional[48] implemented in Vienna *ab initio* simulation package (VASP 6.2.0).[49-51] The electron-ion interactions were modelled utilizing the projector augmented wave (PAW) pseudopotential and the plane wave basis-set was expanded to a converged cut-off energy of 450 eV. The energy calculation was performed using Methfessel-Paxton smearing method with the width of 0.05 eV. The van der Waals interaction was considered by the empirical DFT-D3(BJ) method.[52,53] The adsorption energy (E_{ads}) was calculated by the following equation:

$$E_{ads} = E_{X^*} - E_{surf} - E_X \quad (3)$$

where E_{X^*}, E_{surf}, and E_X are the total energies of the adsorbate on the surface, bare surface, and gaseous adsorbate molecule. The asterisk represents the adsorbate on the surface.

The Gibbs free energy of adsorption (G_{ads}) was calculated by the E_{ads} with the thermodynamic correction under the reaction condition of 413.15 K as follows:

$$G_{ads} = E_{ads} + \Delta ZPE + \Delta(\Delta U) - T\Delta S^{\ominus} + RT + RT\ln\left(\frac{p}{p^{\ominus}}\right) + RT\ln(x_i) \quad (4)$$

where ΔZPE, $\Delta(\Delta U)$, and $\Delta S^{\ominus}$ respectively represent the variation of zero-point energy, internal energy variation, and entropy of the surface adsorbate for the adsorption process under the reaction condition. The thermodynamic corrections were calculated based on the partition functions from Boltzmann distribution. The detailed formulae could be found in our previous work.[54-57] P and $p^{\ominus}$ are the saturated vapor pressure of adsorbate at 413.15 K and the standard vapor pressure, respectively. x_i is the mole fraction of dissolved adsorbate in the liquid water. The negative G_{ads} denotes that the adsorption process is thermodynamically favorable. The more negative G_{ads}, the stronger the adsorption.

The rectangle $p(6\times6)$ supercells of the three-layer exposed Pt(100) and $Pt_1Ni(100)$ surfaces were used to model the exposed facets of $0.2Pt/NiAl_2O_4$ and $0.2Pt5Ni/NiAl_2O_4$, respectively. For the γ-Al_2O_3 and $NiAl_2O_4$ supports, 1 × 1 surface supercells of the (111) facets were employed to represent the corresponding oxide surfaces. In all slab models, a vacuum region of 15 Å was introduced along the surface normal. Monkhorst-Pack k-point meshes of 2 × 2 × 1 were used for the Pt(100) and $Pt_1Ni(100)$ slabs, while a 4 × 4 × 1 meshes was adopted for both γ-Al_2O_3 (111) and $NiAl_2O_4$ (111). The geometry optimization was performed using the conjugate gradient algorithm until the maximal force of all the relaxed atoms lower than 0.05 eV/Å. The transition state was searched using the constrained optimization scheme.[58] and then verified by vibrational analysis, ensuring only one imaginary frequency. During the geometry optimization, the bottom layer metal atoms were fixed, while the upper two-layer surface atoms and adsorbates were allowed to relax.

The LOBSTER code was implemented to perform the Crystal Orbital Hamilton Population

(COHP) analysis[59,60] which is capable of understanding the chemical bonding of BM molecules chemisorbed on the Pt(100) and Pt_1Ni(100) surfaces.[61] The integration of the contribution of the energy bands of the projected crystal orbital Hamilton population up to the Fermi level (IpCOHP) indicates the bonding strength between the functional groups and the surface. To be analogous to the Crystal Orbital Overlap Population (COOP) analysis, -COHP was plotted instead of COHP. Thus, the more negative the -IpCOHP, the stronger the chemical bonding between the adsorbate and the surface.

Data availability

All data generated in this study are provided in the Supplementary Information/Source Data file. Source data are provided with this paper. All data are available from the corresponding author upon request.

Reference

1. Tuck, C.O., Perez, E., Horvath, I.T., Sheldon, R.A. & Poliakoff, M. Valorization of biomass: deriving more value from waste. *Science* **337**, 695-699 (2012).
2. Alonso, D.M.*, et al.* Increasing the revenue from lignocellulosic biomass: Maximizing feedstock utilization. *Sci. Adv.* **3**, e1603301 (2017).
3. Corma, A., Iborra, S. & Velty, A. Chemical routes for the transformation of biomass into chemicals. *Chem. Rev.* **107**, 2411-2502 (2007).
4. Huber, G.W., Iborra, S. & Corma, A. Synthesis of transportation fuels from biomass: chemistry, catalysts, and engineering. *Chem. Rev.* **106**, 4044-4098 (2006).
5. Schutyser, W.*, et al.* Chemicals from lignin: an interplay of lignocellulose fractionation, depolymerisation, and upgrading. *Chem. Soc. Rev.* **47**, 852-908 (2018).
6. Sun, Z., Fridrich, B., De Santi, A., Elangovan, S. & Barta, K. Bright side of lignin depolymerization: toward new platform chemicals. *Chem. Rev.* **118**, 614-678 (2018).

7. Zakzeski, J., Bruijnincx, P.C., Jongerius, A.L. & Weckhuysen, B.M. The catalytic valorization of lignin for the production of renewable chemicals. *Chem. Rev.* **110**, 3552-3599 (2010).
8. Li, C., Zhao, X., Wang, A., Huber, G.W. & Zhang, T. Catalytic transformation of lignin for the production of chemicals and fuels. *Chem. Rev.* **115**, 11559-11624 (2015).
9. Adler, A.*, et al.* Lignin-first biorefining of Nordic poplar to produce cellulose fibers could displace cotton production on agricultural lands. *Joule* **6**, 1845-1858 (2022).
10. Rinaldi, R.*, et al.* Paving the way for lignin valorisation: recent advances in bioengineering, biorefining and catalysis. *Angew. Chem. Int. Ed.* **55**, 8164-8215 (2016).
11. Van den Bosch, S.*, et al.* Reductive lignocellulose fractionation into soluble lignin-derived phenolic monomers and dimers and processable carbohydrate pulps. *Energy Environ. Sci.* **8**, 1748-1763 (2015).
12. Li, N.*, et al.* Selective lignin arylation for biomass fractionation and benign bisphenols. *Nature* **630**, 381-386 (2024).
13. Luo, H.*, et al.* Oxidative Catalytic Fractionation of Lignocellulosic Biomass under Non-alkaline Conditions. *J. Am. Chem. Soc.* **143**, 15462-15470 (2021).
14. Zhu, Y.*, et al.* Oxidative Catalytic Fractionation of Lignocellulose to High-Yield Aromatic Aldehyde Monomers and Pure Cellulose. *ACS Catal.* **13**, 7929-7941 (2023).
15. Shuai, L.*, et al.* Formaldehyde stabilization facilitates lignin monomer production during biomass depolymerization. *Science* **354**, 329-333 (2016).
16. Abu-Omar, M.M.*, et al.* Guidelines for performing lignin-first biorefining. *Energy Environ. Sci.* **14**, 262-292 (2021).
17. Renders, T., Van den Bosch, S., Koelewijn, S.-F., Schutyser, W. & Sels, B. Lignin-first biomass fractionation: the advent of active stabilisation strategies. *Energy Environ. Sci.* **10**, 1551-1557 (2017).
18. Zhai, Y.*, et al.* Depolymerization of lignin via a non-precious Ni–Fe alloy catalyst supported on activated carbon. *Green Chem.* **19**, 1895-1903 (2017).
19. Park, J.*, et al.* Highly efficient reductive catalytic fractionation of lignocellulosic biomass over extremely low-loaded Pd catalysts. *ACS Catal.* **10**, 12487-12506 (2020).
20. Liu, Z.*, et al.* Rational highly dispersed ruthenium for reductive catalytic fractionation of lignocellulose. *Nat. Commun.* **13**, 4716 (2022).
21. Ge, J.*, et al.* Highly efficient metal-acid synergetic catalytic fractionation of lignocellulose under mild conditions over lignin-coordinated N-anchoring Co single-atom catalyst. *Chem. Eng. J.* **462**, 142109 (2023).
22. Brienza, F.*, et al.* Toward a Hydrogen-Free Reductive Catalytic Fractionation of Wheat Straw Biomass. *ChemSusChem* **16**, e202300103 (2023).
23. Chen, J.*, et al.* Efficient fractionation and catalytic valorization of raw biomass in ϵ-caprolactone and water. *ChemSusChem* **16**, e202202162 (2023).
24. Zhang, K.*, et al.* Catalytic Hydrogenolysis of Lignin into Propenyl-monophenol over Ru Single Atoms Supported on CeO_2 with Rich Oxygen Vacancies. *ACS Catal.* **14**, 16115-16126 (2024).
25. Trullemans, L.*, et al.* Renewable and safer bisphenol A substitutes enabled by selective zeolite alkylation. *Nat. Sustain.* **6**, 1693-1704 (2023).
26. Galkin, M.V. & Samec, J.S. Selective route to 2-propenyl aryls directly from wood by a tandem organosolv and palladium-catalysed transfer hydrogenolysis. *ChemSusChem* **7**, 2154-2158 (2014).
27. Li, Y.*, et al.* Hydrogen-Transfer Reductive Catalytic Fractionation of Lignocellulose: High Monomeric Yield

with Switchable Selectivity. *Angew. Chem. Int. Ed.* **62**, e202307116 (2023).

28. Wang, S., Zhang, K., Li, H., Xiao, L.P. & Song, G. Selective hydrogenolysis of catechyl lignin into propenylcatechol over an atomically dispersed ruthenium catalyst. *Nat. Commun.* **12**, 416 (2021).
29. Wang, S., Li, X., Fu, C., Li, H. & Song, G. Atomically Dispersed Palladium Driving Reductive Catalytic Fractionation of Lignocellulose into Alkene-Functionalized Phenols. *ACS Catal.* **14**, 3565-3574 (2024).
30. Zhou, H., Liu, X., Guo, Y. & Wang, Y. Self-hydrogen supplied catalytic fractionation of raw biomass into lignin-derived phenolic monomers and cellulose-rich pulps. *JACS Au* **3**, 1911-1917 (2023).
31. Wang, Y., Zhou, H., Guo, Y. & Liu, X. Method for Preparing Cellulose and Lignin Oil by Depolymerizing Lignocellulose Without Exogenous Hydrogen. WO/2024/124661 A1 [P] (2024).
32. Hannagan, R.T., Giannakakis, G., Flytzani-Stephanopoulos, M. & Sykes, E.C.H. Single-atom alloy catalysis. *Chem. Rev.* **120**, 12044-12088 (2020).
33. Zhang, T., Walsh, A.G., Yu, J. & Zhang, P. Single-atom alloy catalysts: structural analysis, electronic properties and catalytic activities. *Chem. Soc. Rev.* **50**, 569-588 (2021).
34. Nakaya, Y. & Furukawa, S. Catalysis of alloys: classification, principles, and design for a variety of materials and reactions. *Chem. Rev.* **123**, 5859-5947 (2023).
35. Song, W., Du, Q., Li, X., Wang, S. & Song, G. Sustainable Production of Bioactive Molecules from C-Lignin-Derived Propenylcatechol. *ChemSusChem* **15**, e202200646 (2022).
36. Huang, H., Zhang, X., Ma, L. & Liao, Y. Reductive catalytic fractionation of lignocellulose toward propyl- or propenyl-substituted monomers and mechanistic understanding. *Angew. Chem. Int. Ed.* **64**, e202502545 (2025).
37. Liu, Y., Zhang, L., Feng, S. & Chen, X. Promoting Effect of Ni on the Catalytic Production of Alanine from Lactic Acid over RuNi/AC Catalyst. *Ind. Eng. Chem. Res.* **61**, 10285-10293 (2022).
38. Li, D*., et al.* $NiAl_2O_4$ Spinel Supported Pt Catalyst: High Performance and Origin in Aqueous-Phase Reforming of Methanol. *ACS Catal.* **9**, 9671-9682 (2019).
39. Yan, B*., et al.* Dry Reforming of Ethane and Butane with CO2 over $PtNi/CeO_2$ Bimetallic Catalysts. *ACS Catal.* **6**, 7283-7292 (2016).
40. Liu, W*., et al.* Highly-efficient RuNi single-atom alloy catalysts toward chemoselective hydrogenation of nitroarenes. *Nat. Commun.* **13**, 3188 (2022).
41. Kikkawa, S., Teramura, K., Asakura, H., Hosokawa, S. & Tanaka, T. Isolated Platinum Atoms in $Ni/\gamma\text{-}Al_2O_3$ for Selective Hydrogenation of CO_2 toward CH4. *J. Phys. Chem. C* **123**, 23446-23454 (2019).
42. Li, Z*., et al.* Atomically Dispersed Pt on the Surface of Ni Particles: Synthesis and Catalytic Function in Hydrogen Generation from Aqueous Ammonia–Borane. *ACS Catal.* **7**, 6762-6769 (2017).
43. Zhou, H., Song, K., Guo, Y., Liu, X. & Wang, Y. Selective Production of 4-Propylphenol from Lignin Oil without Exogenous Hydrogen over a $RuNi/NiAl_2O_4$ Catalyst. *ACS Sustain. Chem. Eng.* **11**, 15052-15059 (2023).
44. Kayode, G.O. & Montemore, M.M. Factors controlling oxophilicity and carbophilicity of transition metals and main group metals. *Journal of Materials Chemistry A* **9**, 22325-22333 (2021).
45. Li L, Dong L, Li D, Guo Y, Liu X, Wang Y. Hydrogen-Free Production of 4-Alkylphenols from Lignin via Self-Reforming-Driven Depolymerization and Hydrogenolysis. *ACS Catal* **10**, 15197-15206 (2020).
46. Ravel B, Newville M. ATHENA,ARTEMIS,HEPHAESTUS: data analysis for X-ray absorption spectroscopy usingIFEFFIT. *J Synchrotron Radiat* **12**, 537-541 (2005).

47. Scanlon, J.T. & Willis, D.E. Calculation of Flame Ionization Detector Relative Response Factors Using the Effective Carbon Number Concept. *J. Chromatogr. Sci.* **23**, 333-340 (1985).
48. Kresse, G.; Furthmüller, J. Efficiency of ab-initio total energy calculations for metals and semiconductors using a plane-wave basis set. *Comp Mater Sci* **6**, 15-50 (1996.)
49. Kresse, G.; Hafner, J. Ab initio molecular dynamics for liquid metals. . *Phys Rev B Condens Matter* **47**, 558-561 (1993).
50. Kresse, G.; Hafner, J. Ab initio molecular-dynamics simulation of the liquid-metal-amorphous-semiconductor transition in germanium. *Phys Rev B Condens Matter* **49**, 14251-14269 (1994).
51. Kresse, G.; Furthmüller, J. Efficient iterative schemes for ab initio total-energy calculations using a plane-wave basis set. *Physical review B* **54**, 11169 (1996).
52. Grimme, S.; Antony, J.; Ehrlich, S.; Krieg, H. A consistent and accurate ab initio parametrization of density functional dispersion correction (DFT-D) for the 94 elements H-Pu. *J Chem Phy*s **132**, 154104 (2010).
53. Grimme, S.; Ehrlich, S.; Goerigk, L. Effect of the damping function in dispersion corrected density functional theory. *J Comput Chem* **32**, 1456-1465 (2011).
54. Cao, X.-M.; Burch, R.; Hardacre, C.; Hu, P. An understanding of chemoselective hydrogenation on crotonaldehyde over Pt(111) in the free energy landscape: The microkinetics study based on first-principles calculations. *Catal Toda*y **165**, 71-79 (2011).
55. Sun, X.; Cao, X.; Hu, P. Theoretical insight into the selectivities of copper-catalyzing heterogeneous reduction of carbon dioxide. *Sci China-Chem* **58**, 553-564 (2015).
56. Zhang, L.; Shao, Z.-J.; Cao, X.-M.; Hu, P. Insights into different products of nitrosobenzene and nitrobenzene hydrogenation on Pd (111) under realistic reaction conditions. *J Phys Chem C* **122**, 20337-20350 (2018).
57. Hu, W.; Lan, J.; Guo, Y.; Cao, X.-M.; Hu, P. Origin of Efficient Catalytic Combustion of Methane over Co_3O_4(110): Active Low-Coordination Lattice Oxygen and Cooperation of Multiple Active Sites. *ACS Catal* **6**, 5508-5519 (2016).
58. Alavi, A.; Hu, P.; Deutsch, T.; Silvestrelli, P. L.; Hutter, J. CO oxidation on Pt (111): an ab initio density functional theory study. *Phys Rev Lett* **80**, 3650 (1998).
59. Nelson, R.; Ertural, C.; George, J.; Deringer, V. L.; Hautier, G.; Dronskowski, R. LOBSTER: Local orbital projections, atomic charges, and chemical-bonding analysis from projector-augmented-wave-based density-functional theory. *J Comput Chem* **41**, 1931-1940 (2020).
60. Deringer, V. L.; Tchougreeff, A. L.; Dronskowski, R. Crystal orbital Hamilton population (COHP) analysis as projected from plane-wave basis sets. *J Phys Chem A* **115**, 5461-5466 (2011).
61. Zhang, L.; Cao, X.-M.; Hu, P. Insight into chemoselectivity of nitroarene hydrogenation: a DFT-D3 study of nitroarene adsorption on metal surfaces under the realistic reaction conditions. *Appl Surf Sci* **392**, 456-471 (2017).

Acknowledgements

The authors thank the financially supports by the National Key Research and Development Program of China (2022YFA1504903, 2022YFA1504904, 2023YFA1507601) (Y.Q.W.) and

assistance with XAS measurement from Canadian Light Source.

Author contributions Statement

H.Z., Z.R.G., K.P.S., X.H.L., and Y.G.: preparation and characterization of catalysts, and performing the catalytic reactions. Q.X. and X.M.C.: DFT calculations. M.S. and Y.F.H.: collection and analysis of XAS data. X.M.C. and Y.Q.W.: overall direction of the project. H.Z., Q.X., X.M.C. and Y.Q.W. wrote the manuscript with the help from all authors.

Competing Interests Statement

The authors declare no competing interests.

Table 1. SCF of birch wood over various PtNi catalysts.

Table 2. Reaction pathway of lignin model compound SG at different reaction times.

Figure 1. Electron microscopy characterization of 0.2Pt5Ni catalyst. (a) HAADF-STEM image, (b) corresponding EDS-mapping images of Pt, Ni, Al, and O elements, (c) AC- HAADF-STEM image with corresponding lattice fringe, (d) enlarged STEM image of c.

Figure 2. Fine-structure characterizations of PtNi catalysts. (a) In situ CO-DRIFTS spectra of 2Pt/$NiAl_2O_4$, 5Ni/$NiAl_2O_4$, 2Pt5Ni, and 0.2Pt5Ni catalysts. (b) Pt L_3-edge XANES spectra and (c) EXAFS Fourier–transform spectra of various samples. k^2-weighted wavelet transforms for the Pt L_3-edge XAFS signals of (d) Pt foil, (e) 0.2Pt5Ni sample, and (f) PtO_2 based on Morlet wavelets (The data are not phase-corrected).

Figure 3. Time profile of birch SCF reaction over 0.2Pt5Ni catalyst.

Figure 4. The comparative diagram of the reaction pathways. (a) energy profiles for C_α-OH deH, C_α-OH deOH-I, and C_α-OH deOH-II on $Pt_1Ni(100)$. (b) corresponding the molecular structure diagram. The Pt atoms in $Pt_1Ni(100)$ have been circled in red in the last figure.

Figure 5. Proposed mechanism of lignin depolymerization in SCF.

Editorial summary:
Making phenols from lignocellulose without added hydrogen is attractive but typically requires high metal loadings and yields mostly saturated products. A single-atom Pt1Ni alloy converts birch sawdust to phenolic monomers with high yield and propenyl selectivity while leaving cellulose intact.

Peer Review Information: *Nature Communications* thanks Yu Jing, Mingyang Liu, and Zhicheng Luo for their contribution to the peer review of this work. A peer review file is available.